Strain-Controlled Current Switching in Weyl Semimetals

S. M. Rafi-Ul-Islam,* Zhuo Bin Siu,† Chi Sun, and Mansoor B. A. Jalil‡

Department of Electrical and Computer Engineering, National University of Singapore, Singapore

Applying strain to a Weyl semimetal (WSM) breaks its lattice symmetry and results in a valley-dependent strain gauge potential. Here, we investigate the application of the strain potential to modulate the valley and charge transport of a WSM-based n-p-n junction system. The strain potential, in combination with insulating barriers, enables modulation of the current and the realization of valley-asymmetric transmission with a high on:off ratio. By considering the geometric optics of electron waves and the transverse displacement of Fermi surfaces due to the strain gauge, we derive the critical strains for switching the current, as well as for the onset of complete angular separation of the two valley currents. The analytical results are verified by numerical calculations of the tunneling transmission and conductance. We also derive the expression for the subthreshold swing of the device, which can achieve values below the thermionic limit by tuning the strain and barrier height.

I. INTRODUCTION

Extensive research is currently underway into gapless two-dimensional materials such as graphene [1–3] and silicene [4–6], whose linear dispersion near the Dirac points can be described by the relativistic Dirac equation [7]. These materials have drawn much attention owing to their exotic characteristics, such as gapless energy spectra [3], high mobility, extraordinary quantum Hall effect [8,9], and Klein tunneling [10,11]. However, the absence of a band gap and the inability to fully modulate the conductance due to Klein tunneling make graphene inappropriate for most electronic switching devices except in high-frequency applications [12–18]. There have been attempts to artificially induce band gaps in graphene by means such as geometrical confinement [19]. However, these methods tend to degrade the electron mobility [20]. A recently discovered topological state named the Weyl semimetal (WSM) can be considered as the three-dimensional analogue of graphene with a linear dispersion relation at low energies but much higher carrier mobility [21]. Several exotic characteristics have also been theoretically predicted and experimentally observed in WSM materials [22–24]. A WSM possesses helical electron and holelike states touching each other at points named Weyl nodes in three-dimensional k space [22,25–28]. The presence of all three Pauli matrices in the low-energy Hamiltonian

about the vicinity of the Weyl points confers mobility and robustness against perturbations to WSMs [29]. Unlike graphene, the topological states in WSMs are preserved by the translational properties of the crystal structure [30]. However, similar to graphene, the presence of Klein tunneling [10,31–35] in pristine WSM adversely affects the conductance modulation, and thus the suitability of WSMs for switching purposes. To resolve this issue, several approaches ranging from band gap modulation [36] to chemical deposition [37] have been proposed. However, all these approaches come with drawbacks, such as mobility degradation and fabrication complexity. We thus propose an alternative way to manipulate the transmission gap in WSMs by utilizing strain [38,39]. Strain can be induced locally in WSMs by applying tension on an appropriate substrate rather than on the WSM material itself [40–42]. The application of strain breaks the lattice symmetry and induces valley-dependent gauge potentials in WSMs. Strain is used in combination with a barrier potential, the latter of which cannot suppress Klein tunneling on its own. However, strain-induced gauge fields can achieve this by displacing the Fermi surface and thus overcome the switching limitations of Dirac-like materials. The gauge fields also allow electron transmission to be modulated in a valley-dependent manner. By considering the geometric optics of electron waves, we show that the application of strain can result in the complete angular separation of the two valleys, as well as a high on:off current ratio. Strain engineering also allows the modulation of the transmission gap, which is useful in optimizing the switching characteristics of our WSM-based device.

*e0021595@u.nus.edu
†elesiuz@nus.edu.sg
‡elembaj@nus.edu.sg

II. MODEL AND THEORETICAL APPROACH

We consider a *n-p-n* junction based on a WSM under the effects of strain. The schematic of our proposed model is shown in Fig. 1. A metallic point source analogous to the tip of a scanning tunneling microscope injects electrons with net propagation along the *x* direction. Such a point source can either be induced electrostatically or patterned lithographically [14]. Different regions in the WSM can be made into either *p* or *n* type by applying back-gate voltages. Insulating barriers are placed at the first *n-p* junction, and subtend an angle of β_b at the point source. These act to block transmission for electrons with incident angles greater than β_b. Such barriers have been proposed in a graphene *p-n* junction in Ref. [14]. In that work, the barriers were placed close to the normal incident direction to block Klein tunneling, which occurs predominantly close to normal incidence, and thus suppress the *off* current. However, there are drawbacks to this approach, as there is significant leakage current from off-normal incidence contributions as well as reduction of the *on* current, resulting in a low on:off ratio. In contrast, in our proposed model, the barriers block incident angles well away from normal, thus ensuring a large *on* current. The *off* current is suppressed by the combination of the barriers and the application of strain, which causes a valley-dependent shift of the Fermi surfaces, as we explain later. An important component of our proposed setup is the application of strain to the central region in order to modulate the valley-dependent electron transmission. There are various ways to induce localized strain in the desired segment of the Weyl semimetal devices, e.g., by applying strain through heteroepitaxial lattice mismatch [43] and dislocations [44], light-induced shear strain [45], compressive strain due to strong pinning of substrate [46], and back-gate voltage-induced strain [47]. The WSM material can also be continuously deformed by controlling the above competing interactions by a combination of a scanning tunneling microscopy prob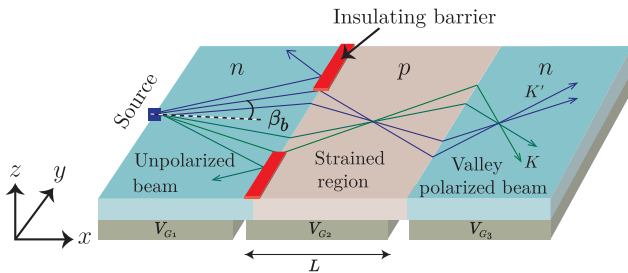e tip and the electric field from a back-gate electrode. Such probe tip–induced deformation results in a localized strain field in the WSM lattice [47,48]. Uniaxial lattice strain can be induced by applying tension to the substrate beneath the central region. The resulting lattice deformation modifies the nearest-neighbor hopping parameters [49] and breaks the lattice symmetry. These effects can be modeled by introducing a strain gauge potential [50–53] $A_s(r) = A(0, 1, 0)$, where A is a parameter proportional to the size of the strain. For instance, in Cd_3As_2, $A = 0.0372 \, \eta u_{32}$ eV^{-1} Å^{-2}, where $\eta = \pm 1$ is the valley index and u_{32} is the Cauchy strain tensor component [54]. It has been experimentally shown that several WSM candidate materials such as Cd_3As_2 and Na_3Bi can attain strains of up to the critical values of 1.3% and 7.0%, respectively, where the rotational symmetry of their crystal lattice and hence the existence of Weyl points are preserved [55]. Moreover, it has been shown experimentally that terahertz light pulses can be used to induce terahertz frequency inter-layer shear strain on a Weyl semimetal of up to 2% uniaxial strain amplitude, resulting in an equivalent gauge potential in the range of 3–39 meV [45]. Another experimental group demonstrated a strain gauge field in the region of 5 to 55 meV in $MoTe_2$ [56]. Recently, one group reported that a critical strain of 112 meV can be applied to a WSM without compromising its crystal integrity [57]. The WSM junction can be described by the Hamiltonian

$$H_\eta = v_F \vec{\sigma} \cdot \left(\vec{p} + \frac{\eta \vec{A}_s}{v_F} \right) + V_0 \sigma_0, \quad (1)$$

where $v_F = 1.5 \times 10^6$ ms^{-1} is the Fermi velocity, $\vec{\sigma} = (\sigma_x, \sigma_y, \sigma_z)$ are the Pauli matrices, σ_0 is the 2×2 identity matrix, $\vec{p} = (p_x, p_y, p_z)$ are the momentum operators along the *x*, *y*, and *z* directions respectively, and $\eta = \pm 1$ denotes the *K* and *K'* valleys, respectively. Here V_0 is the electrostatic potential difference between the *n* and *p* regions, which can be modulated by the back-gate voltages $V_{G_{1-3}}$ in the three regions. [We have made the approximation that the system is infinitely thick in the *z* direction and neglected the quantum confinement effects. Several groups have experimentally shown that in moderately thick (e.g., greater than 25 nm) WSM samples, quantum confinement and transmission quenching effects are negligible [45,58,59]. Recently, the WSM phase has been shown to be preserved in strained WSM (Cd_3As_2) films with thickness of 80 nm [59].] The respective wave functions in the *n* and *p* regions can be expressed as

$$\psi_\pm^{n/p}(x, y, z) = e^{i(\pm k_x^{n/p} x + k_y^{n/p} y + k_z^{n/p} z)}$$

$$\times \left(1, \frac{k_x^{n/p} + i k_y^{n/p}}{k_z^{n/p} + (\epsilon_n - V_0^{n/p})/v_F} \right)^\top, \quad (2)$$

where $\psi_+^{n/p}$ and $\psi_-^{n/p}$ denote the forward propagating and reflected waves in the different segments, respectively, ϵ_n

FIG. 1. Schematic diagram of *n-p-n* WSM junction with strained central region. A metallic point source injects valley unpolarized electrons into the central part of the device. Because of the strain-induced valley-dependent gauge fields that result in a negative refractive index, electrons associated with the *K* and *K'* valleys experience angular separation in the drain region.

is the Fermi energy, and n and p indicate the unstrained source and drain and strained central regions, respectively. The model is translationally invariant along the y and z directions, so that $k_y^p = k_y^n + \eta A_s$ and $k_z^p = k_z^n$. The Fermi wavevectors in the n and p regions can be expressed as

$$(k_F^{n/p})^2 = (k_x^{n/p})^2 + (k_y^{n/p})^2 + (k_z^{n/p})^2$$
$$= \left(\frac{\epsilon_n - V_0^{n/p}}{v_F} \right)^2. \tag{3}$$

On account of the strain, the central segment wavevectors k_x^p and k_y^p become valley dependent. The incident azimuthal and polar angles in the source n region are given by $\phi = \tan^{-1}(k_y^n/k_x^n)$ and $\gamma = \tan^{-1}(k_z^n \cos\phi/k_x^n)$, respectively. The corresponding refracted angles in the p-type central region are given by $\theta = \tan^{-1}(k_y^p/k_x^p)$ and $\alpha = \tan^{-1}(k_z^p \cos\theta/k_x^p)$. The total wave function in a specific region can be expressed as a linear combination of the forward propagating and reflected waves. The valley-dependent transmission probability T_η of the system can be found by imposing wave function continuity at the interfaces $x = 0$ and $x = L$.

In Fig. 2 we show geometric ray diagrams corresponding to the electron trajectories in the system. As mentioned earlier, two insulating barriers are inserted at the $x = 0$ interface and extend along the transverse $\pm y$ directions, leaving a gap at the center that subtends an angle β_b with respect to the point source. Such insulating barriers can be realized by using electron beam lithography [14,60]. Any electron beam incident upon the interface at an angle larger than β_b will be blocked by the barriers. Thus, in the absence of strain-induced gauge fields (i.e., the on state), carrier transmission is restricted to the incident angular

range $-\beta_b < \phi < \beta_b$ [see Fig. 2(a)]. At normal incidence, electrons can be transmitted to the drain region without any backscattering due to Klein tunneling, thus resulting in a relatively large on current. In the off state, strain is applied to the central region and electrons experience the strain-induced gauge potential A_s there. This causes the electrons to be deflected away from normal incidence. The transverse deflection is in opposite directions for the two valleys. If the magnitude of A_s is large enough, electron transmission in the K and K' valleys is restricted to $\phi > \beta_b$ and $\phi < -\beta_b$, respectively. Under this situation, the presence of insulating barriers results in electrons of all incidence angles being reflected, and hence no current is detected at the drain lead, leading to the off state [see Fig. 2(b)]. This forms the basis of the strain-controlled conductance switch in the WSM system. The strain-induced transverse displacement and the resulting switch between the on and off states can be explained by the kinematical analysis [61] of the incidence and refraction angles in the k_x-k_y plane, as shown in Fig. 3. For the on state in the absence of strain, the Fermi surfaces in the leads and central segment with radii $(\epsilon_n - V_0^{n/p})/v_F$ are all aligned and centered on the same $k_y = 0$ axis. The central Fermi surface has a different radius from that in the source and drain leads due to the different gate potentials $V_0^{n/p}$. The dashed line parallel to the k_x axis in Fig. 3(a) reflects the conservation of transverse momentum k_y during the transmission process. In the off state, the strain gauge potentials shift the Fermi surfaces of the strained WSM along opposite transverse $\pm k_y$ directions for the K and K' valleys. Therefore, the Fermi surfaces of the strained central region corresponding to the K and K' valleys take the form of two circles with the same radii $(\epsilon_n - V_0^p)/v_F$, but centered at different points $(0, \pm A_s/v_F, 0)$, as illustrated in Fig. 3(b). A sufficiently large magnitude of A_s displaces the central Fermi surfaces away from the k_x axis such that there is no transmission for incidence angles $|\phi| < \beta_b$. In other words, the conservation of transverse momentum (represented by the overlap between the Fermi surfaces of the source and central regions) can only occur for incidence angles $|\phi| >$
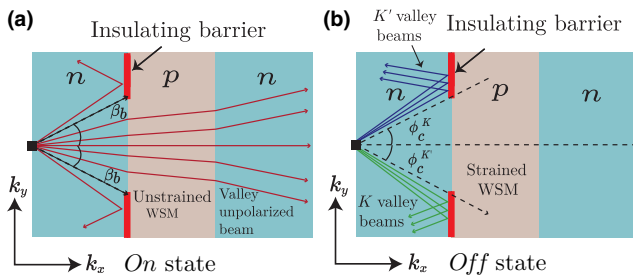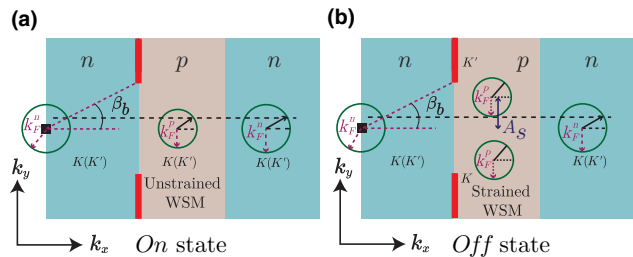

FIG. 2. Schematic illustration of the switching mechanism of our proposed model. (a) The on state occurs in the absence of strain. All rays with incident angles less than either the blocking angle, i.e., $|\phi| < \beta_b$, are transmitted through the central region and collected in the drain region. The transmitted current is valley unpolarized. (b) The off state is obtained under strain such that $|\phi_c^{K/K'}| \geq \beta_b$, where β_b is the blocking angle. Therefore, total internal reflection occurs for incident angles within the range $-\beta_b < \phi < \beta_b$, while reflection at the insulating barriers occurs for $|\phi| > \beta_b$, thus resulting in the suppression of transmission for all angles.

FIG. 3. Schematic of the kinematical construction of the electronic transmission through the WSM junctions in the k_x-k_y plane for the (a) on state and (b) off state.

β_b, which are blocked by the insulating barriers. Therefore, the transmission is blocked, resulting in the *off* state. In Fig. 3(b) we depict the situation at the threshold strain value at the onset of the *off* state. The conservation of k_y, k_z and energy yields the following relation between the incident and refracted angles:

$$\left[\sqrt{(\epsilon_n - V_0{}^p)^2 - (\epsilon_n - V_0{}^n)^2 \sin^2 \gamma}\right] \sin \theta - v_F \eta A_s$$
$$= (\epsilon_n - V_0{}^n) \cos \gamma \sin \phi. \qquad (4)$$

The above relation has a valley (η) dependence, which in turn leads to the valley dependence of the electron propagation. To view this schematically, the variation of the refracted angles with respect to the incident angles are plotted in Fig. 4 for different strain values. In the *on* state, i.e., in the absence of the strain gauge potential, there is no valley dependence and the refracted angles for both the K and K' valleys are identical. Hence, both the K and K' valley electrons follow the same trajectories, which results in valley-independent transmission. Moreover, electrons at normal incidence ($\phi = 0$) are also transmitted at normal incidence ($\theta = 0$). This coincides with the conventional Klein tunneling that is marked by the absence of backscattering at normal incidence. The resulting maximal transmission of carriers ensures a large *on* current. In addition, we get only positive (negative) refractive angles for positive (negative) incident angles. This phenomenon corresponds to the presence of only positive refractive indices in the system in the absence of strain. Note that transmission is blocked for incident angles exceeding the blocking angle set by the insulating barriers, i.e., $|\phi| > \beta_b = \pi/3$, and this applies for all strain
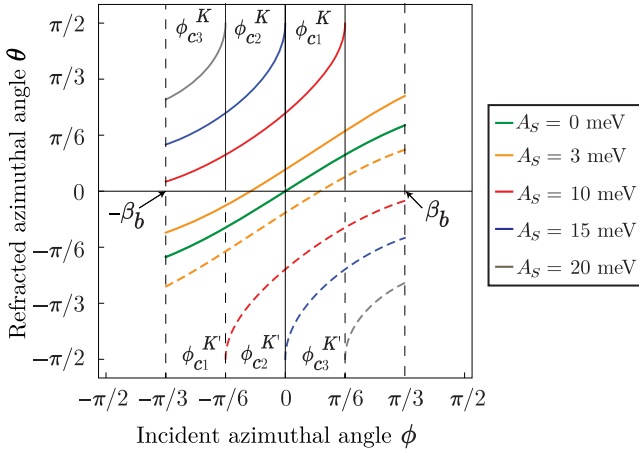

FIG. 4. Relation between incidence and refraction angles under different strain gauge field strengths, with $\gamma = 0$, $\epsilon_n = 10$ meV, and $V_0^p = 25$ meV. The blocking angle is set at $|\beta_b| = \pi/3$. The upper and lower halves represent the K (solid line) and K' (dotted line) valleys, respectively. Any incident angle greater than the blocking angle $|\beta_b|$ is blocked by the insulating barriers.

values. A different picture arises when a strain gauge field is applied. As mentioned earlier, the gauge field has the effect of displacing the Fermi surfaces of the two valleys in opposite directions in k space along the transverse k_y axis. This results in a split of the incident electron beam into two valley-dependent refracted beams because of the unequal refracted angles for the two valleys (see the curve corresponding to $A_s = 3$ meV in Fig. 4). As the strength of the strain field is increased, a range of incident angles is blocked due to total internal reflection. From Eq. (4), the strain and valley-dependent critical angles for the two valleys are given by

$$\phi_c^{K/K'} = \eta \sin^{-1}\left(\frac{\chi - v_F A_s}{(\epsilon_n - V_0^n) \cos \gamma}\right), \qquad (5)$$

where $\chi = \sqrt{(\epsilon_n - V_0^p)^2 - (\epsilon_n - V_0^n)^2 \sin^2 \gamma}$ and $\eta = +1$ (-1) corresponds to the K (K') valley. The critical angles corresponding to the two valleys are of opposite signs, e.g., at $A_s = 10$ meV, $\phi_c^K = \pi/6$ and $\phi_c^{K'} = -\pi/6$. In combination with the insulating barriers, the transmitted K and K' electrons are limited to the incident angular range $-\beta_b < \phi < \phi_c^K$ and $\phi_c^{K'} < \phi < \beta_b$, respectively. With a further increase in the strain strength, we reach a strain value where the critical angle $\phi_c^{K,K'}$ goes to zero. This critical strain-induced gauge is given by

$$|A_c| = \frac{\sqrt{(\epsilon_n - V_0^p)^2 - (\epsilon_n - V_0^n)^2 \sin^2 \gamma}}{v_F}. \qquad (6)$$

For the parameters in Fig. 4, A_c corresponds to $A_s = 15$ meV. Here A_c marks the onset of perfect coupling between the transmitted incident angle and the valley degree of freedom. As shown in Fig. 4, the allowed angular ranges span $-\beta_b < \phi < 0$ ($0 < \phi < \beta_b$) for the K (K') valley. Under this condition, only electrons with negative (positive) incidence angles are transmitted for the K (K') valley, and hence the transmitted angular ranges for the two valleys are mutually exclusive. Furthermore, the system exhibits the phenomenon of negative refractive index, in which a K valley electron with a negative incident angle is transmitted at a positive angle, and vice versa for the other valley. We also observe that, when the strain gauge potential exceeds A_c, there is a transmission gap for incident angles $\phi_c^K < \phi < \phi_c^{K'}$ in addition to the existing gap for $|\phi| > \beta_b$ due to the insulating barriers. For instance, in Fig. 4, at $A_s = 20$ meV, which exceeds the critical value of $A_c = 15$ meV, we have a transmission gap extending over $\phi_{c3}^K < \phi < \phi_{c3}^{K'}$. This transmission gap widens with increasing A_s. At some value of A_s, we have a situation where $|\phi_c^{K/K'}| \geq \beta_b$, such that the transmission gap extends over the entire range of incident angles ϕ. Hence, there is zero transmission into the central segment and the
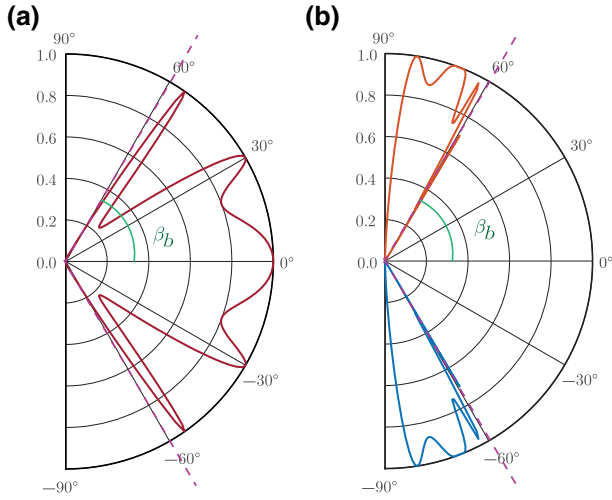
FIG. 5. Transmission profiles for the K and K' valleys with two different strain values (a) $A_s = 0$ meV, (b) $A_s = 23.5$ meV. The red and blue curves represent the K' and K valley transmissions, respectively. The parameters used are $\gamma = 0$, $\epsilon_n = 10$ meV, and $V_0^p = 25$ meV. The dotted lines correspond to the angles $\phi = \pm\beta_b$ subtended by the insulating barriers.

device switches to the *off* state. The strain gauge field corresponding to this switch can be expressed as

$$A_{\text{switch}}^{\min} = (v_F)^{-1} \left[\sqrt{(\epsilon_n - V_0^p)^2 - (\epsilon_n - V_0^n)^2 \sin^2 \gamma} \right.$$
$$\left. - (\epsilon_n - V_0^n) \sin \beta_b \cos \gamma \right]. \quad (7)$$

In Fig. 5 we plot the angular dependence of the carrier transmission, which exhibits strong valley and strain dependence. Here, we fix the energy and barrier height but vary the strain strength to demonstrate the switching operation more clearly. In the absence of any strain gauge field, the transmission profiles for the K and K' valleys coincide with each another, and both are symmetric with respect to the incident angle $\phi = 0$, as shown in Fig. 5(a). Perfect carrier transmission of $T = 100\%$ occurs at normal incidence, which is a signature of the conventional Klein tunneling. This coincides with our *on* state. The

petal-like spikes in the transmission spectra correspond to the resonant condition $k_x^p L = n\pi$, where n is an integer and L is the width of the barrier region. Under the application of a sufficiently strong strain (such that $A_s > A_c$), the transmission profiles corresponding to the two valleys exhibit a complete angular separation, as illustrated in Fig. 5(b). The carrier transmission probability decreases significantly, almost to zero, in the vicinity of normal incidence. There is a transmission gap within the angular interval $\phi_c^K < \phi < \phi_c^{K'}$ (corresponding to approximately $-60° < \phi < 60°$). Within this incident angle range, the wavevector in the central segment k_x^p is imaginary, so the wave function there becomes evanescent. Thus, we have total internal reflection at the interface. There are still transmission windows in the incident angular range $-\beta_b < \phi < \phi_c^K$ ($\phi_c^{K'} < \phi < \beta_b$) for the K (K') valley. However, with a further increase in strain (i.e., $A_s \geq A_{\text{switch}}^{\min}$) such that $\phi_c^\eta \geq \beta_b$, the total suppression of electron transmission occurs. This defines the *off* state of our device and ensures a minimal level of leakage current. The large Klein tunneling current in the *on* state and almost total suppression of the current in the *off* state translates into a very large on:off ratio. The energy gap in transmission and its modulation by strain A_s and barrier height $V_0^{n/p}$ are plotted in Fig. 6. In the presence of strain in the central segment, the transmission is blocked over a certain range of electron energy. The transmission energy gap becomes wider with a larger strain potential [Fig. 6(a)]. This trend is consistent with the larger transverse shift of the Fermi circle of the central region with increasing strain gauge potential (see Fig. 3). Thus, we require a much larger Fermi level shift in order to increase the radii of the Fermi surfaces of the three regions so as to achieve overlap in k_y between the Fermi surfaces. In Fig. 6(b) we show the effect of varying the barrier height $V_0^{n/p}$ in modulating the transmission gap. The increase in $V_0^{n/p}$ does not broaden the transmission gap, but merely displaces the center of the transmission gap. The latter trend may be readily explained by the fact that the transmission gap occurs when there is internal reflection of the electron wave function, a condition which arises when k_x^p is imaginary. From Eq. (3), we find that
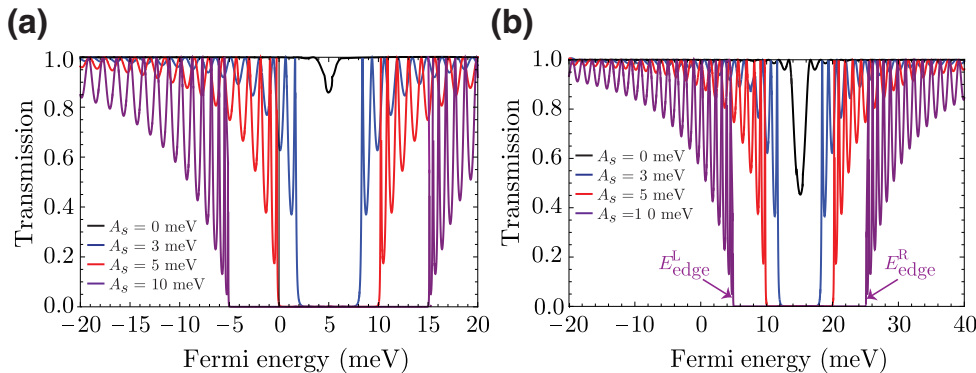

FIG. 6. Transmission profile with respect to Fermi energy (ϵ_n) for different strain (A_s) and barrier height ($V_0^{n/p}$) values for the normal incidence case with $\gamma = 0$ and (a) $V_0^p = 5$ meV and (b) $V_0^p = 15$ meV with $V_0^n = 0$ meV.
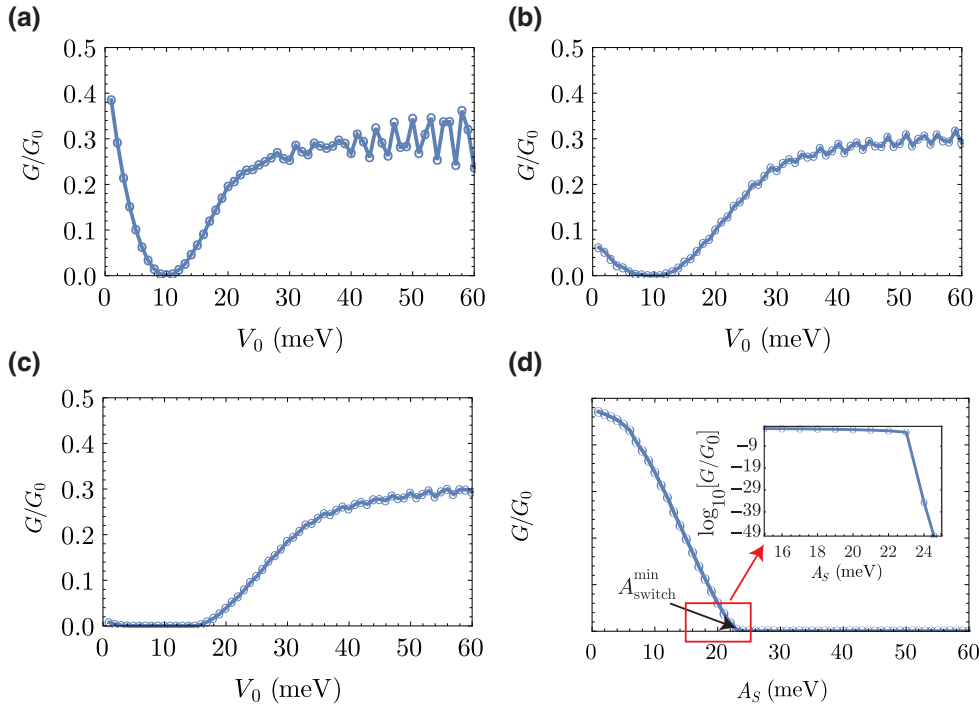
FIG. 7. Dependence of the conductance G on the barrier height (V_0^p) for various strain magnitudes with $\epsilon_n = 10$ meV, $V_0^n = 0$ meV, and blocking angle $\beta_b = \pi/3$. (a) $A = 0$ meV, (b) $A_s = 10$ meV (c) $A_s = 15$ meV, and (d) G as a function of A_s for $V_0^p = 25$ meV.

k_x^p is a function of ($\epsilon_n - V_0^p$), thus explaining the role of the barrier potential V_0^p in displacing the transmission gap along the electron energy axis. To explain the strain modulation of the transmission gap, we consider the maximum of the valence band (i.e., left edge of the transmission gap) and the minimum of the conduction band (i.e., right edge of the transmission gap). The analytical expression for these can be obtained from Eq. (5) by setting $\phi_c = \beta_b$, which yields

$$E_{\text{edge}}^{L/R} = \sec^2 \beta_b [V_0^p \sec^2 \gamma - v_F A_s \sec \gamma \sin \beta_b$$
$$- V_0^n(\sin^2 \beta_b + \tan^2 \gamma) + \zeta \Omega], \quad (8)$$

where $\Omega = \sec^2 \gamma (\lambda^2 - v_F^2 A_s^2 - \rho)^{1/2}$ with $\lambda = v_F A_s \sec \gamma + (V_0^n - V_0^p) \sin \beta_b$ and $\rho = (V_0^n - V_0^p)^2 \tan^2 \gamma$. Here E_{edge}^L and E_{edge}^R denote the left and right edges of the transmission gap, respectively, and likewise $\zeta = \pm 1$ corresponds to the two edges of the gap. By taking the difference between the two, the strain-dependent transmission gap is given by

$$\Delta \epsilon = 2 \sec^2 \beta_b (\sec^2 \gamma \{[v_F A_s \sec \gamma + (V_0^n - V_0^p) \sin \beta_b]^2$$
$$- (v_F^2 A_s^2) - (V_0^n - V_0^p)^2 \tan^2 \gamma \})^{1/2}. \quad (9)$$

The above analytical expressions for the transmission gap and its left and right edges are in agreement with the numerical results shown in Fig. 6. Finally, we integrate the transmission over all the incident angles to obtain

the *on* and *off* currents of the device, and the strain-controlled switching between the two states. The ballistic conductance of the device G is obtained from the integral [10]

$$G = G_0 \int_{-\beta_b}^{\beta_b} T_\eta(\epsilon_n - V_0^{n/p}, k_y^{n/p}) \cos \phi \, d\phi$$
$$\times \int_{-\pi/2}^{\pi/2} \cos^2 \gamma \, d\gamma \int_{-\infty}^{\infty} \left(-\frac{\partial f}{\partial \epsilon_n} \right) d\epsilon_n, \quad (10)$$

where f is the Fermi-Dirac distribution function and $G_0 = e^2 L_x L_y k_F^2 / 8\pi^3$ is the unit of quantum conductance (L_y and L_z are the device length and width, respectively). We consider here the low-temperature limit so that the temperature derivative of the Fermi-Dirac distribution can be considered as a Dirac delta function. (See Appendix A for details of the conductance variation at different finite temperatures.) The allowed range of incident angles for our device is limited to $-\beta_b < \phi < \beta_b$ rather than the general limit $-\pi/2 < \phi < \pi/2$, as mentioned in Eq. (10). In Fig. 7(a) we show the conductance for the *n*-*p*-*n* junction device in the absence of any gauge potentials (i.e., $A_s = 0$). In the absence of strain gauge fields, there is no conductance gap, although the conductance drops to zero at the specific value of gate potential $V_0 = V_0^p - V_0^n$, which coincides with the Fermi energy ϵ_n (in this special case, the resulting Fermi surface in the central *p* region reduces to a point, resulting in zero conductance). However, a conductance gap develops under the influence of the strain gauge field A_s, as

shown in Figs. 7(b) and 7(c). In the presence of A_s, the conductance is reduced significantly, especially for $V_0^p < \epsilon_n$. A distinct conductance gap is seen, centered around ϵ_n. In Fig. 7(d), the conductance is plotted as a function of the gauge field for a specific barrier height (V_0^p) and Fermi energy (ϵ_n). The conductance falls exponentially to almost zero when $A_s \geq A_{\text{switch}}^{\min}$, where transmission is blocked for all incident angles. The strong suppression of conductance beyond $A_{\text{switch}}^{\min}$ improves the figure of merit of our transistor, i.e., its $I_{\text{on}}/I_{\text{off}} = G_{A_s=0}/G_{A_s=A_{\text{switch}}^{\min}}$ ratio. This ratio can be calculated numerically using the Landauer formalism [62] stated in Eq. (10), and in our assumed range of parameters yields an $I_{\text{on}}/I_{\text{off}}$ ratio of the order of 10^{25} [see the inset of Fig. 7(d)]. Additionally, the strain-induced gauge potential also modulates the subthreshold swing (S_{sub}) of the WSM-based switch. From Eq. (8), we can derive the formula for the SS as

$$
\begin{aligned}
S_{\text{sub}} = {} & \frac{k_B T}{q} \ln(10) \cos^2 \beta_b \cos^2 \gamma \\
& \times \left(1 - \frac{(V_0^p - V_0^n)(\sin^2 \beta_b + \tan^2 \gamma) - v_F A_s}{\Omega} \right)^{-1}.
\end{aligned}
\tag{11}
$$

Equation (11) shows the dependence of the SS on the strain parameter (A_s). The $[k_B T \ln(10)/q]$ term of Eq. (11) is the conventional thermionic limit of 60 mV/Dec [63], while the strain-dependent factor represents the modification of the S_{sub}. By tuning the strain gauge field and the barrier height, we can obtain a S_{sub} less than 60 mV/Dec. In conventional (i.e., nontunneling-based) transistors, the S_{sub} has a lower limit of 60 mV/Dec (at room temperature) due to diffusion-driven transport, which results in high static power dissipation. In contrast, the application of strain allows our device to beat the thermionic power limit, thus paving the way for low power dissipation.

III. CONCLUSION

In conclusion, we propose a strained WSM-based n-p-n junction system to achieve good switching and valley filtering characteristics by exploiting the transverse gauge potentials arising from the applied strain. The strain-induced gauge fields cause opposite displacements of the Fermi surfaces for the K and K' valleys, while the introduction of insulating barriers allows us to manipulate the carrier trajectories by blocking certain incident angles. The combination of strain and insulating barriers enables modulation of the transmission leading to the angular splitting of the two valley currents and a high on:off ratio. The *on* current is kept high by exploiting the Klein tunneling effect, while the transmission gap can be tuned to suppress the *off* current to a negligible level. We analytically derive the critical strains for switching the current, as well as for the onset of complete angular separation of the two valley

currents. The analytical results are verified by numerical calculations of the tunneling transmission and conductance. Finally, we derive the subthreshold swing and show that it can be tuned by strain and barrier potential to break the thermionic limit of 60 mV/Dec.

ACKNOWLEDGMENTS

APPENDIX: FINITE TEMPERATURE EFFECTS ON CONDUCTANCE

In Fig. 7 of the main text, we considered the low-temperature limit where the temperature derivative of the Fermi-Dirac distribution can be approximated as a Dirac delta function. Here, we plot the conductances at different finite temperatures to explain the effect of temperature on the device characteristics (see Fig. 8). At the low temperature of 1 K, the conductance falls sharply with the increase of strain values [Fig. 8(a)]. Moreover, a very small *off* current is found in the vicinity of $A_s = 22.5$ meV, which is an excellent match with the critical strain estimated from Eq. (7) in the main text. At 10 K in Fig. 8(b), we see similar trends as in Fig. 8(a) as the temperature and hence the carrier thermal energy are very low. However, the situation becomes different at higher temperatures when the carrier thermal energy is no longer negligible. In Figs. 8(c) (100 K) and 8(d) (298 K), we note two significant changes in the conductance variations. Firstly, the *on* current slightly decreases, and the conductance slowly falls with the increase of strain amplitudes up to a certain value. Secondly, the strain-induced gauge potential required to restrict the junction conductance to a negligible limit (i.e., on the order of 10^{-7}) is much higher than the gauge field in the low temperature case. This increment of the strain potential values needed to switch off the channel is required to nullify the higher thermal carrier energy associated with the higher temperature. As a rule of thumb, the required critical strain needed for switching at room temperature is on the order of $A_{\text{switch}}^{\min} + 3k_B T$, where k_B and T denote the Boltzmann constant and temperature in kelvins, respectively. In the low temperature range, the on:off ratio yields large values. A similar order of on:off ratio can be obtained at room temperature settings by using higher strain-induced gauge potential values. For example, at room temperature, an on:off ratio on the order of 10^7 can be obtained with a strain gauge potential on the order of 95 meV [see Fig. 8(d)]. Recently, one group reported that a critical strain of 112 meV can be applied to
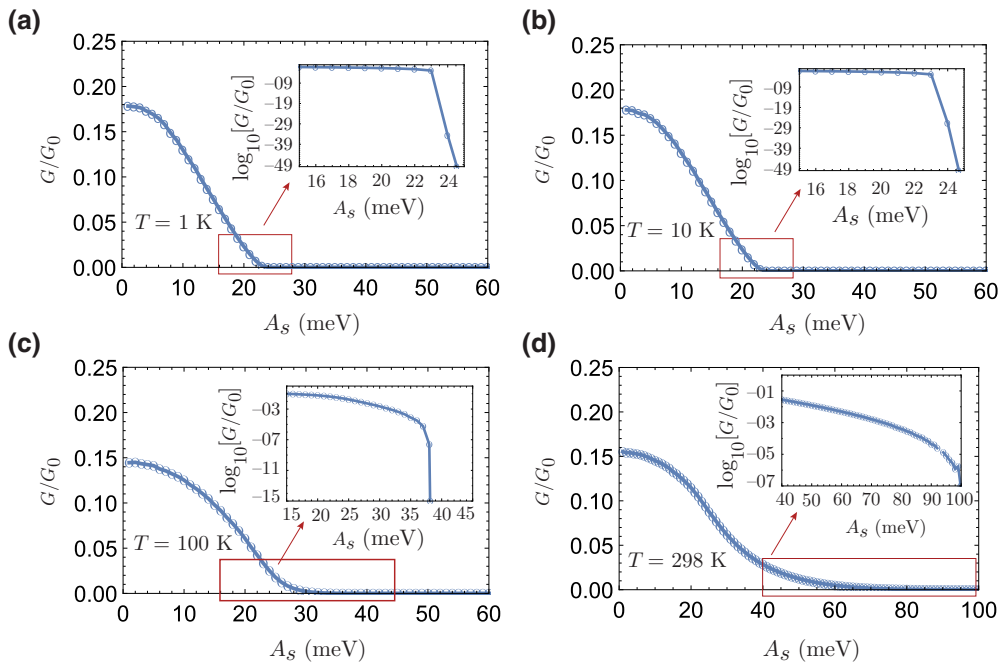
FIG. 8. Dependence of the conductance G on the strain amplitude A_s at (a) $T = 1$ K, (b) $T = 10$ K, (c) $T = 100$ K, and (d) $T = 298$ K. The insets are enlarged versions of certain ranges of strain values. The common parameters used are $\epsilon_n = 10$ meV, $V_0^n = 0$ meV, $V_0^p = 25$ meV, and blocking angle $\beta_b = \pi/3$.

the WSM without compromising its crystal integrity [57], which is sufficient for switching our device even at room temperature.

[1] E. Hwang and S. D. Sarma, Acoustic phonon scattering limited carrier mobility in two-dimensional extrinsic graphene, Phys. Rev. B **77**, 115449 (2008).

[2] K. I. Bolotin, K. Sikes, Z. Jiang, M. Klima, G. Fudenberg, J. Hone, P. Kim, and H. Stormer, Ultrahigh electron mobility in suspended graphene, Solid State Commun. **146**, 351 (2008).

[3] K. S. Novoselov, D. Jiang, F. Schedin, T. Booth, V. Khotkevich, S. Morozov, and A. K. Geim, Two-dimensional atomic crystals, Proc. Natl. Acad. Sci. **102**, 10451 (2005).

[4] C.-C. Liu, W. Feng, and Y. Yao, Quantum Spin Hall Effect in Silicene and Two-Dimensional Germanium, Phys. Rev. Lett. **107**, 076802 (2011).

[5] P. Vogt, P. De Padova, C. Quaresima, J. Avila, E. Frantzeskakis, M. C. Asensio, A. Resta, B. Ealet, and G. Le Lay, Silicene: Compelling Experimental Evidence for Graphenelike Two-Dimensional Silicon, Phys. Rev. Lett. **108**, 155501 (2012).

[6] M. Ezawa, A topological insulator and helical zero mode in silicene under an inhomogeneous electric field, New J. Phys. **14**, 033003 (2012).

[7] C. Beenakker, Colloquium: Andreev reflection and Klein tunneling in graphene, Rev. Mod. Phys. **80**, 1337 (2008).

[8] K. S. Novoselov, A. K. Geim, S. Morozov, D. Jiang, M. Katsnelson, I. Grigorieva, S. Dubonos, and A. Firsov, Two-dimensional gas of massless Dirac fermions in graphene, Nature **438**, 197 (2005).

[9] Y. Zhang, Y.-W. Tan, H. L. Stormer, and P. Kim, Experimental observation of the quantum Hall effect and Berry's phase in graphene, Nature **438**, 201 (2005).

[10] C. Yesilyurt, S. G. Tan, G. Liang, and M. B. Jalil, Klein tunneling in Weyl semimetals under the influence of magnetic field, Sci. Rep. **6**, 38862 (2016).

[11] M. Katsnelson, K. Novoselov, and A. Geim, Chiral tunnelling and the Klein paradox in graphene, Nat. Phys. **2**, 620 (2006).

[12] U. Coskun, M. Brenner, T. Hymel, V. Vakaryuk, A. Levchenko, and A. Bezryadin, Distribution of Supercurrent Switching in Graphene under the Proximity Effect, Phys. Rev. Lett. **108**, 097003 (2012).

[13] F. Zhai, Y. Ma, and Y.-T. Zhang, A valley-filtering switch based on strained graphene, J. Phys. Condens. Matter **23**, 385302 (2011).

[14] R. N. Sajjad and A. W. Ghosh, High efficiency switching using graphene based electron "optics", Appl. Phys. Lett. **99**, 123101 (2011).

[15] T. Kawai, M. Poetschke, Y. Miyamoto, C. Rocha, S. Roche, and G. Cuniberti, Mechanically-induced transport switching effect in graphene-based nanojunctions, Phys. Rev. B **83**, 241405 (2011).

[16] K. Sääskilahti, A. Harju, and P. Pasanen, Gate-controlled current switch in graphene, Appl. Phys. Lett. **95**, 092104 (2009).

[17] B. Standley, W. Bao, H. Zhang, J. Bruck, C. N. Lau, and M. Bockrath, Graphene-based atomic-scale switches, Nano Lett. **8**, 3345 (2008).

[18] Y. Wu, K. A. Jenkins, A. Valdes-Garcia, D. B. Farmer, Y. Zhu, A. A. Bol, C. Dimitrakopoulos, W. Zhu, F. Xia, and P. Avouris, State-of-the-art graphene high-frequency electronics, Nano Lett. **12**, 3062 (2012).

[19] N. Meng, J. F. Fernandez, D. Vignaud, G. Dambrine, and H. Happy, Fabrication and characterization of an epitaxial graphene nanoribbon-based field-effect transistor, IEEE Trans. Electron Devices **58**, 1594 (2011).

[20] Q. Wilmart, S. Berrada, D. Torrin, V. H. Nguyen, G. Fève, J.-M. Berroir, P. Dollfus, and B. Plaçais, A Klein-tunneling transistor with ballistic graphene, 2D Mater. **1**, 011006 (2014).

[21] R. D. Hills, A. Kusmartseva, and F. Kusmartsev, Current-voltage characteristics of Weyl semimetal semiconducting devices, Veselago lenses, and hyperbolic Dirac phase, Phys. Rev. B **95**, 214103 (2017).

[22] X. Wan, A. M. Turner, A. Vishwanath, and S. Y. Savrasov, Topological semimetal and Fermi-arc surface states in the electronic structure of pyrochlore iridates, Phys. Rev. B **83**, 205101 (2011).

[23] H. Weng, C. Fang, Z. Fang, B. A. Bernevig, and X. Dai, Weyl Semimetal Phase in Noncentrosymmetric Transition-Metal Monophosphides, Phys. Rev. X **5**, 011029 (2015).

[24] S.-Y. Xu, N. Alidoust, I. Belopolski, Z. Yuan, G. Bian, T.-R. Chang, H. Zheng, V. N. Strocov, D. S. Sanchez, G. Chang, *et al.*, Discovery of a Weyl fermion state with Fermi arcs in niobium arsenide, Nat. Phys. **11**, 748 (2015).

[25] X. Wan, A. Turner, A. Vishwanath, and S. Y. Savrasov, Electronic structure of pyrochlore iridates: From topological Dirac metal to Mott insulator, arXiv preprint arXiv:1007.0016 (2010).

[26] A. Burkov and L. Balents, Weyl Semimetal in a Topological Insulator Multilayer, Phys. Rev. Lett. **107**, 127205 (2011).

[27] S. Rafi-Ul-Islam, Z. B. Siu, C. Sun, and M. bin Abdul Jalil, Realization of Weyl semimetal phases in topoelectrical circuits, New J. Phys. **22**, 023025 (2020).

[28] S. Rafi-Ul-Islam, Z. B. Siu, and M. B. Jalil, Topoelectrical circuit realization of a Weyl semimetal heterojunction, Commun. Phys. **3**, 1 (2020).

[29] C. Yesilyurt, Z. B. Siu, S. G. Tan, G. Liang, and M. B. Jalil, Conductance modulation in Weyl semimetals with tilted energy dispersion without a band gap, J. Appl. Phys. **121**, 244303 (2017).

[30] Y. Yang, C. Bai, X. Xu, and Y. Jiang, Shot noise and electronic properties in the inversion-symmetric Weyl semimetal resonant structure, Nanotech. **29**, 074002 (2018).

[31] T. O'Brien, M. Diez, and C. Beenakker, Magnetic Breakdown and Klein Tunneling in a type-II Weyl Semimetal, Phys. Rev. Lett. **116**, 236401 (2016).

[32] C. Bai, Y. Yang, and K. Chang, Chiral tunneling in gated inversion symmetric Weyl semimetal, Sci. Rep. **6**, 21283 (2016).

[33] M. Van Delft, S. Pezzini, T. Khouri, C. Müller, M. Breitkreiz, L. M. Schoop, A. Carrington, N. Hussey, and S. Wiedmann, Electron-Hole Tunneling Revealed by Quantum Oscillations in the Nodal-Line Semimetal HfSiS, Phys. Rev. Lett. **121**, 256602 (2018).

[34] S. Li, A. Andreev, and B. Spivak, Klein tunneling and magnetoresistance of *pn* junctions in Weyl semimetals, arXiv preprint arXiv:1605.02799 (2016).

[35] S. Rafi-Ul-Islam, Z. B. Siu, and M. B. Jalil, Anti-Klein tunneling in topoelectrical Weyl semimetal circuits, Appl. Phys. Lett. **116**, 111904 (2020).

[36] M. Y. Han, B. Özyilmaz, Y. Zhang, and P. Kim, Energy Band-Gap Engineering of Graphene Nanoribbons, Phys. Rev. Lett. **98**, 206805 (2007).

[37] R. Balog, B. Jørgensen, L. Nilsson, M. Andersen, E. Rienks, M. Bianchi, M. Fanetti, E. Lægsgaard, A. Baraldi, S. Lizzit, *et al.*, Bandgap opening in graphene induced by patterned hydrogen adsorption, Nat. Mater. **9**, 315 (2010).

[38] T. Fujita, M. Jalil, and S. Tan, Valley filter in strain engineered graphene, Appl. Phys. Lett. **97**, 043508 (2010).

[39] D. Pikulin, A. Chen, and M. Franz, Chiral Anomaly from Strain-Induced Gauge Fields in Dirac and Weyl Semimetals, Phys. Rev. X **6**, 041021 (2016).

[40] T. Rauch, S. Achilles, J. Henk, and I. Mertig, Spin Chirality Tuning and Topological Semimetals in Strained HgTe$_x$S$_{1-x}$, Phys. Rev. Lett. **114**, 236805 (2015).

[41] D. Wang, L. Chen, X. Wang, G. Cui, and P. Zhang, The effect of substrate and external strain on electronic structures of stanene film, Phys. Chem. Chem. Phys. **17**, 26979 (2015).

[42] F. Guinea, M. Katsnelson, and A. Geim, Energy gaps and a zero-field quantum Hall effect in graphene by strain engineering, Nat. Phys. **6**, 30 (2010).

[43] I. Zeljkovic, D. Walkup, B. A. Assaf, K. L. Scipioni, R. Sankar, F. Chou, and V. Madhavan, Strain engineering Dirac surface states in heteroepitaxial topological crystalline insulator thin films, Nat. Nanotechnol. **10**, 849 (2015).

[44] Y. Liu, Y. Li, S. Rajput, D. Gilks, L. Lari, P. Galindo, M. Weinert, V. Lazarov, and L. Li, Tuning Dirac states by strain in the topological insulator Bi$_2$Se$_3$, Nat. Phys. **10**, 294 (2014).

[45] E. J. Sie, C. M. Nyby, C. Pemmaraju, S. J. Park, X. Shen, J. Yang, M. C. Hoffmann, B. Ofori-Okai, R. Li, A. H. Reid, *et al.*, An ultrafast symmetry switch in a Weyl semimetal, Nat. **565**, 61 (2019).

[46] J. Hass, R. Feng, T. Li, X. Li, Z. Zong, W. De Heer, P. First, E. Conrad, C. Jeffrey, and C. Berger, Highly ordered graphene for two dimensional electronics, Appl. Phys. Lett. **89**, 143106 (2006).

[47] S. Zhu, Y. Huang, N. N. Klimov, D. B. Newell, N. B. Zhitenev, J. A. Stroscio, S. D. Solares, and T. Li, Pseudo-magnetic fields in a locally strained graphene drumhead, Phys. Rev. B **90**, 075426 (2014).

[48] N. N. Klimov, S. Jung, S. Zhu, T. Li, C. A. Wright, S. D. Solares, D. B. Newell, N. B. Zhitenev, and J. A. Stroscio, Electromechanical properties of graphene drumheads, Science **336**, 1557 (2012).

[49] F. Zhai and L. Yang, Strain-tunable spin transport in ferromagnetic graphene junctions, Appl. Phys. Lett. **98**, 062101 (2011).

[50] Z.-Z. Cao, Y.-F. Cheng, and G.-Q. Li, Strain-controlled electron switch in graphene, Appl. Phys. Lett. **101**, 253507 (2012).

[51] V. M. Pereira and A. C. Neto, Strain Engineering of Graphene's Electronic Structure, Phys. Rev. Lett. **103**, 046801 (2009).

[52] V. M. Pereira and A. H. C. Neto, All-graphene integrated circuits via strain engineering, arXiv preprint arXiv:0810.4539 (2008).

[53] F. Zhai, X. Zhao, K. Chang, and H. Xu, Magnetic barrier on strained graphene: A possible valley filter, Phys. Rev. B **82**, 115442 (2010).

[54] Z. Xu, Z. B. Siu, Y. Chen, J. Huang, Y. Li, C. Sun, C. Yesilyurt, and M. B. Jalil, Group delay time and Harttman effect in strained Weyl semimetals, J. Phys. Condsen. Matter **32**, 035301 (2020).

[55] S. Guan, Z.-M. Yu, Y. Liu, G.-B. Liu, L. Dong, Y. Lu, Y. Yao, and S. A. Yang, Artificial gravity field, astrophysical Analogues, and Topological Phase Transitions in Strained Topological Semimetals, npj Quantum Mater. **2**, 1 (2017).

[56] Y. Sun, S.-C. Wu, M. N. Ali, C. Felser, and B. Yan, Prediction of Weyl semimetal in orthorhombic MoTe$_2$, Phys. Rev. B **92**, 161107 (2015).

[57] T. Bzdušek, A. Rüegg, and M. Sigrist, Weyl semimetal from spontaneous inversion symmetry breaking in pyrochlore oxides, Phys. Rev. B **91**, 165105 (2015).

[58] H. Ma, P. Chen, B. Li, J. Li, R. Ai, Z. Zhang, G. Sun, K. Yao, Z. Lin, and B. Zhao, Thickness-tunable synthesis of ultrathin type-II Dirac semimetal PtTe2 single crystals and their thickness-dependent electronic properties, Nano Lett. **18**, 3523 (2018).

[59] M. Goyal, H. Kim, T. Schumann, L. Galletti, A. A. Burkov, and S. Stemmer, Surface states of strained thin films of the Dirac semimetal Cd$_3$As$_2$, Phys. Rev. Mater. **3**, 064204 (2019).

[60] Q. H. Wang and M. C. Hersam, Room-temperature molecular-resolution characterization of self-assembled organic monolayers on epitaxial graphene, Nat. Chem. **1**, 206 (2009).

[61] L. Dell'Anna and A. De Martino, Wave-vector-dependent spin filtering and spin transport through magnetic barriers in graphene, Phys. Rev. B **80**, 155416 (2009).

[62] T. Sohier and B. Yu, Ultralow-voltage design of graphene PN junction quantum reflective switch transistor, Appl. Phys. Lett. **98**, 213104 (2011).

[63] R. N. Sajjad and A. W. Ghosh, Manipulating chiral transmission by gate geometry: Switching in graphene with transmission gaps, ACS Nano **7**, 9808 (2013).